
This manuscript has been submitted for publication in EARTH AND PLANETARY SCIENCE LETTERS. Please note that this is a preprint listed on EarthArXiv which has not undergone full peer review yet. Subsequent versions may have slightly different content. If accepted, the final version of this manuscript will be available via the ‘Peer-reviewed Publication DOI’ link on the right-hand side of this webpage. Please feel free to contact any of the authors; we welcome the feedback.

1

Rapid fault healing after seismic slip

2 John D. Bedford^{1*}, Takehiro Hirose¹ and Yohei Hamada¹

3 ¹Kochi Institute for Core Sample Research (X-star), Japan Agency for Marine-Earth Science and
4 Technology (JAMSTEC), 200 Monobe-otsu, Nankoku, Kochi 783-8502, Japan

5 *Corresponding author: John Bedford (j.bedford@jamstec.go.jp)

6

7 **Highlights**

- 8
- We experimentally investigate fault healing after high-velocity slip
- 9
- Gabbro and granite fault gouges dynamically weaken at high slip velocity
- 10
- Once slip has ceased, the gouges rapidly recover their strength
- 11
- Enhanced healing is caused by thermally activated chemical bonding

12 **Abstract**

13 Fault strength recovery (healing) following an earthquake is a key process in controlling the recurrence of
14 future events; however, the rates and mechanisms of fault healing are poorly constrained. Here, by
15 performing high-velocity friction experiments at seismic slip rates (0.57 m/s), we show that granite and
16 gabbro fault gouges recover their strength rapidly after experiencing dynamic weakening. The healing rates
17 are two orders of magnitude faster than those observed in typical frictional healing experiments performed
18 at slow slip velocities (micrometers to millimeters per second). Analysis of the sheared gouges using Raman
19 spectroscopy suggests that enhanced healing after seismic slip is associated with thermally activated
20 chemical bonding at frictional contacts in the gouge. Our results imply that seismogenic faults regain their
21 strength early during interseismic periods, indicating that healing may not be the dominant control on
22 earthquake recurrence, with other processes, such as far-field tectonic loading or frictional stability
23 transitions, likely dictating the occurrence of future events.

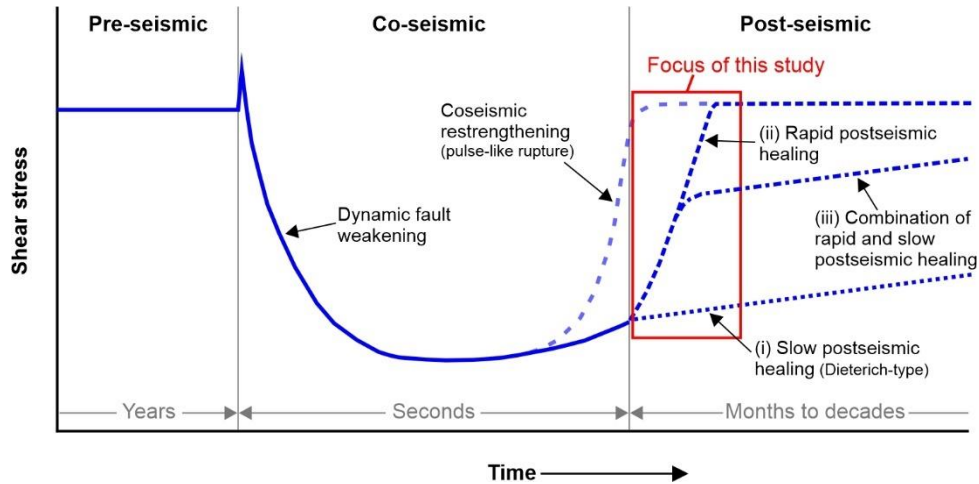
24

25 **1. Introduction**

26 Faults slip suddenly during earthquakes, accelerating to velocities on the order of a few meters per
27 second. At these seismic slip velocities a significant reduction in fault strength occurs (Di Toro et al., 2011)
28 as a result of various dynamic weakening mechanisms becoming activated by shear heating (e.g., Tullis,
29 2015). Although our knowledge of dynamic fault weakening processes has increased significantly over the
30 last 25 years since the advent of high-velocity friction experiments (Tsutsumi and Shimamoto, 1997), our
31 understanding of how faults regain their strength after dynamic weakening, once seismic slip has ceased, is
32 more limited. Fault restrengthening is a fundamental process in the earthquake cycle that may control the
33 recurrence time (Vidale et al., 1994), the maximum strength that can be attained (Kanamori and Allen,
34 1986; Scholz et al., 1986), and the nature of radiated energy (McLaskey et al., 2012) in future events.

35 The rate of fault restrengthening can vary with both time and space along the fault during the earthquake
36 cycle (Li et al., 2006; Pei et al., 2019). Restrengthening may occur initially during coseismic slip itself, as
37 sometimes observed during the deceleration phase of high-velocity friction experiments (Harbord et al.,
38 2021; Proctor et al., 2014; Sone and Shimamoto, 2009; Violay et al., 2019). Coseismic restrengthening
39 (Fig. 1) is a potentially important process in the generation of pulse-like earthquake ruptures (Heaton,
40 1990), which require that faults rapidly regain their strength (self-heal) after the passage of the rupture front.
41 However, the mechanisms of coseismic restrengthening are poorly constrained and it is a phenomenon that
42 is not always observed in experiments, or it may only partially recover the strength lost during high-velocity
43 fault slip (Boulton et al., 2017; Han et al., 2007; Hunfeld et al., 2021; Seyler et al., 2020; Yao et al., 2013).
44 In such cases, the majority of fault restrengthening must occur in the postseismic regime instead, when the
45 fault is held in quasi-stationary contact.

46 The process of strength recovery as a fault is held in quasi-stationary contact, known as fault healing,
47 has been extensively studied in experiments performed at slow sliding velocities, on the order of
48 micrometers per second (Marone and Saffer, 2015). The common procedure for studying fault healing in
49 the laboratory is to perform slide-hold-slide (SHS) experiments (Dieterich, 1972; Marone, 1997), whereby
50 the shearing of fault materials is paused for predetermined durations and then shear strength is monitored
51 as sliding is resumed after the hold period. Previous low-velocity SHS experiments have shown that
52 frictional strength increases linearly with the logarithm of hold time, with healing rate being dependent on
53 the composition of the fault materials (Carpenter et al., 2016). The physical mechanisms responsible for
54 fault healing are debated, with time-dependent growth of real contact area due to asperity creep often
55 invoked to explain healing behavior (Dieterich and Kilgore, 1994). However, more recent work has
56 suggested other processes such as chemical bond formation could be responsible for fault healing observed
57 in laboratory experiments (Li et al., 2011; Thom et al., 2018).



58

59 **Figure 1:** Schematic diagram of fault strength evolution during the seismic cycle. During coseismic slip, a
 60 significant reduction in shear stress occurs as a result of dynamic fault weakening. In the postseismic
 61 regime the fault regains its strength as it is held in quasi-stationary contact. The aim of this study is to
 62 determine whether fault strength recovery immediately following seismic slip occurs via (i) slow
 63 “Dieterich-type” healing, (ii) rapid postseismic healing, or (iii) a combination of rapid and slow healing.

64

65 In some specific cases, the healing rates determined from low-velocity SHS experiments correlate well
 66 with stress drops observed during sequences of small repeating earthquakes in nature (i.e., the magnitude
 67 of the stress drop increases as the duration of the recurrence interval increases (Marone et al., 1995; Vidale
 68 et al., 1994)). However, following large earthquakes, geophysical observations suggest that rapid fault
 69 restrengthening can occur in comparison to typical recurrence intervals, with the majority of the strength
 70 being recovered early during the interseismic period. For example, shear-wave splitting measurements
 71 following the 1995 Kobe earthquake (moment magnitude M_w 6.9) on the Nojima fault indicate that the
 72 majority of fault strength had recovered within 33 months of the main event (recurrence interval of
 73 approximately 2000 years) (Tadokoro and Ando, 2002). Borehole permeability measurements from the
 74 Longmenshan fault zone that hosted the 2008 Wenchuan earthquake (M_w 7.9), suggest that the fault healed
 75 within 0.6 to 2.5 years after the earthquake (Xue et al., 2013). Seismic velocity measurements made

76 following the same event, and also the nearby 2013 Lushan earthquake (M_w 6.6), support the notion of rapid
77 healing on the fault (Pei et al., 2019), with similar enhanced strength recovery rates also inferred after the
78 2004 Parkfield earthquake (M_w 6.0) on the San Andreas fault (Li et al., 2006) and between the 2019
79 Ridgecrest earthquake pair (M_w 6.4 and M_w 7.1) in the eastern California shear zone (Magen et al., 2020).
80 Geophysical observations thus potentially indicate that different postseismic healing processes are in
81 operation immediately following large earthquakes, leading to more rapid restrengthening, than the classic
82 “Dieterich-type” healing mechanisms (Dieterich, 1972; Dieterich and Kilgore, 1994) responsible for fault
83 strengthening in low-velocity SHS experiments (Fig. 1). It should also be noted that over typical recurrence
84 intervals of large earthquakes (up to several hundreds of years), processes such as pressure solution will
85 increase cohesion of fault materials, contributing to the long-term strength evolution of the fault during
86 interseismic periods (Muhuri et al., 2003; Tenthorey and Cox, 2006; van den Ende and Niemeijer, 2019).

87 In order to investigate rapid postseismic healing processes in the laboratory we need to simulate
88 earthquake slip velocities, something that is not done in typical low-velocity SHS experiments. By shearing
89 at seismic slip velocities, the fault materials will also experience dynamic weakening (Di Toro et al., 2011),
90 which more closely mimics what happens during natural earthquakes. Here, we perform high-velocity (0.57
91 m/s) SHS experiments on gabbro and granite gouges under room humidity conditions at a constant normal
92 stress of 1.5 MPa in all experiments, to investigate how the gouges regain their strength during quasi-
93 stationary hold periods after experiencing dynamic weakening. We varied the length of the static hold
94 period in order to determine whether the postseismic restrengthening behavior exhibits either, (i)
95 “Dieterich-type” healing as observed in low-velocity SHS experiments, (ii) a form of more rapid healing,
96 or (iii) a combination of rapid and slow healing; as shown schematically in Figure 1. We then analyze the
97 microstructures of the sheared gouges and perform Raman spectroscopy in an attempt elucidate the
98 underlying healing mechanisms in operation after seismic slip events.

99

100

101 2. Methods

102 *2.1. Experimental procedure*

103 The experimental samples were produced by crushing and sieving intact samples of Inada granite
104 and Belfast gabbro to form simulated fault gouges (powders) with grain sizes between 63-125 μm . A layer
105 of simulated gouge (measured by weight to produce a layer with an initial thickness of 1.5 mm) was then
106 sandwiched between two cylindrical stainless steel experimental forcing blocks (diameter = 25 mm). The
107 surface of the blocks contains radial grooves (0.5 mm deep) to minimize boundary shear between the gouge
108 layer and the forcing blocks during the experiments. To limit gouge loss during shearing, the gouge layer
109 was contained laterally by a 5 mm thick polytetrafluoroethylene (PTFE) sleeve (Fig. S1). The low-friction
110 PTFE sleeve was cut and tightened onto the forcing blocks using a hose clip (Fig. S1), following the
111 procedure outlined in the supplementary material of De Paola et al., (2015). We used a torque-screwdriver
112 to ensure the hose clip was tightened by the same amount for each experiment. Once the gouge sample was
113 constructed in between the forcing blocks, it was sheared using the PHV rotary shear apparatus (Tanikawa
114 et al., 2012) in the Rock Mechanics Laboratory at the Kochi Institute for Core Sample Research (Japan).

115 Before the main SHS experiment, the gouge samples were pre-sheared for four complete
116 revolutions (equivalent to 0.2 m of slip) under a normal stress of 0.75 MPa at a rate of 1.7 mm/s, to ensure
117 the gouge layer thickness was even across the sample. The normal stress was then increased to the
118 experimental target value of 1.5 MPa. As all experiments were run under the same normal stress we did not
119 correct for the shear stress contribution from the PTFE sleeve, with previous work showing that the
120 mechanical contribution from the PTFE is negligible (Seyler et al., 2020). All tests were conducted under
121 room temperature (22-25 $^{\circ}\text{C}$) and humidity (30-50%) conditions. During the main SHS experiments the
122 gouge layers were sheared at 650 rpm for 285 revolutions (slide 1), they were then held in quasi-stationary
123 contact for a predetermined amount of time, before being sheared again for another 285 revolutions at 650
124 rpm (slide 2). As the slip velocity varies with radial position, we use an “equivalent slip velocity” (v_e)

125 which corresponds to the velocity at 2/3 of the radius of the cylindrical specimens (De Paola et al., 2015),
126 given by:

$$127 \quad v_e = \frac{4\pi Rr}{3}$$

128 where R is the revolution rate of the motor and r is the sample radius. In our experiments, a revolution rate
129 of 650 rpm corresponds to an equivalent slip velocity of 0.57 m/s. During each sliding event the gouge layer
130 was sheared for 285 revolutions which corresponds to an equivalent slip displacement (d_e) of ~15 m ($d_e =$
131 $v_e t$ where t is time).

132 In some of the high-velocity experiments temperature measurements were made by placing
133 thermocouples next to the upper surface of the gouge layer (<0.5 mm above the gouge surface). Two holes
134 were drilled into the upper experimental forcing block (on the stationary side of the fault) and
135 thermocouples were inserted into the holes and sealed into place using a ceramic bond. The thermocouples
136 were positioned at 2/3 of the radius so that the temperature measurements were consistent with the
137 calculated v_e and d_e .

138 As well as the high-velocity SHS experiments, some additional tests were performed at
139 micrometer-per-second slip velocities to compare healing rates after low-velocity slip with the rates
140 determined in our high-velocity experiments (Fig. 3). In the low-velocity SHS experiments (performed at
141 an equivalent slip velocity of $2.6 \mu\text{m}\cdot\text{s}^{-1}$) we used intact cylindrical rock-to-rock samples of Inada granite
142 and Belfast gabbro, instead of gouge. Initially we tried performing the low-velocity SHS experiments using
143 gouge samples, however, we found negligible healing even after hold periods >1000 s (healing rate, $\beta \approx$
144 0). We believe this is due to the low normal stress conditions and also low shear strain the gouge had
145 experienced before the low-velocity SHS experiments were performed. We tried to perform experiments
146 where the gouges were sheared at millimeter-per-second slip velocities to an equivalent slip displacement
147 of 15 m prior to the low-velocity SHS tests (i.e., the same d_e as achieved in the high-velocity SHS
148 experiments), however, there was a large amount of gouge extrusion from between the PTFE ring and the

149 metal forcing blocks during the pre-shearing. Therefore, as the purpose of our low-velocity SHS
150 experiments is just to provide an approximate representation of typical healing rates at slow sliding
151 velocities, we chose to instead include data from rock-to-rock samples in Fig. 3, as the healing rates we
152 determined from the rock-to-rock samples are close to typical healing rates observed in many low-velocity
153 healing studies (Carpenter et al., 2016; Marone, 1997). Prior to the low-velocity SHS experiments, the
154 cylindrical rock samples were rotated for more than 1000 rotations at a constant speed of 4 rpm ($v_e = 3.5$
155 $\text{mm}\cdot\text{s}^{-1}$) over a range of incrementally increasing normal stresses from 0.3 to 1.4 MPa. The purpose of this
156 procedure was to remove any heterogeneities and ensure the surfaces on opposite side of the sliding
157 interface were parallel. The wear materials produced on the sliding surface during this pre-sliding were not
158 removed before the SHS experiments, thus the rock samples were separated by a thin gouge layer during
159 the experiments. The wear materials produced during the experiments were allowed to extrude from the
160 slip zone (we did not use a PTFE containing ring for these tests). Once the sliding surface was prepared,
161 the normal stress was increased to 1.5 MPa and the samples were sheared for 0.26 mm during each sliding
162 event in the SHS experiment at a velocity of $2.6 \mu\text{m}\cdot\text{s}^{-1}$; the length of the hold time between the sliding
163 events was varied to determine the healing rate.

164

165 **2.2. Raman spectroscopy**

166 After the experiments the PTFE ring was removed and the sample holders were gently opened to
167 expose the sheared gouge sample. The surface of the gouge was then analyzed using Raman spectroscopy.
168 (Note that Raman spectra were acquired on the exposed gouge surface before it was impregnated with
169 epoxy resin and prepared for microstructural imaging). Raman spectra of the test samples were obtained
170 with a 514.5 nm Ar laser (Showa Optronics Co., Ltd.) and T64000 Raman system (Jobin Yvon Horiba).
171 The laser passed through a 40 \times objective and the laser power at the sample surface was set at 2–5 mW. The
172 scattered light was collected by backscattered geometry with a 25 μm pinhole and a holographic notch filter,
173 and finally dispersed using a 1800 grids/mm grating and analyzed by a Peltier cooled CCD detector

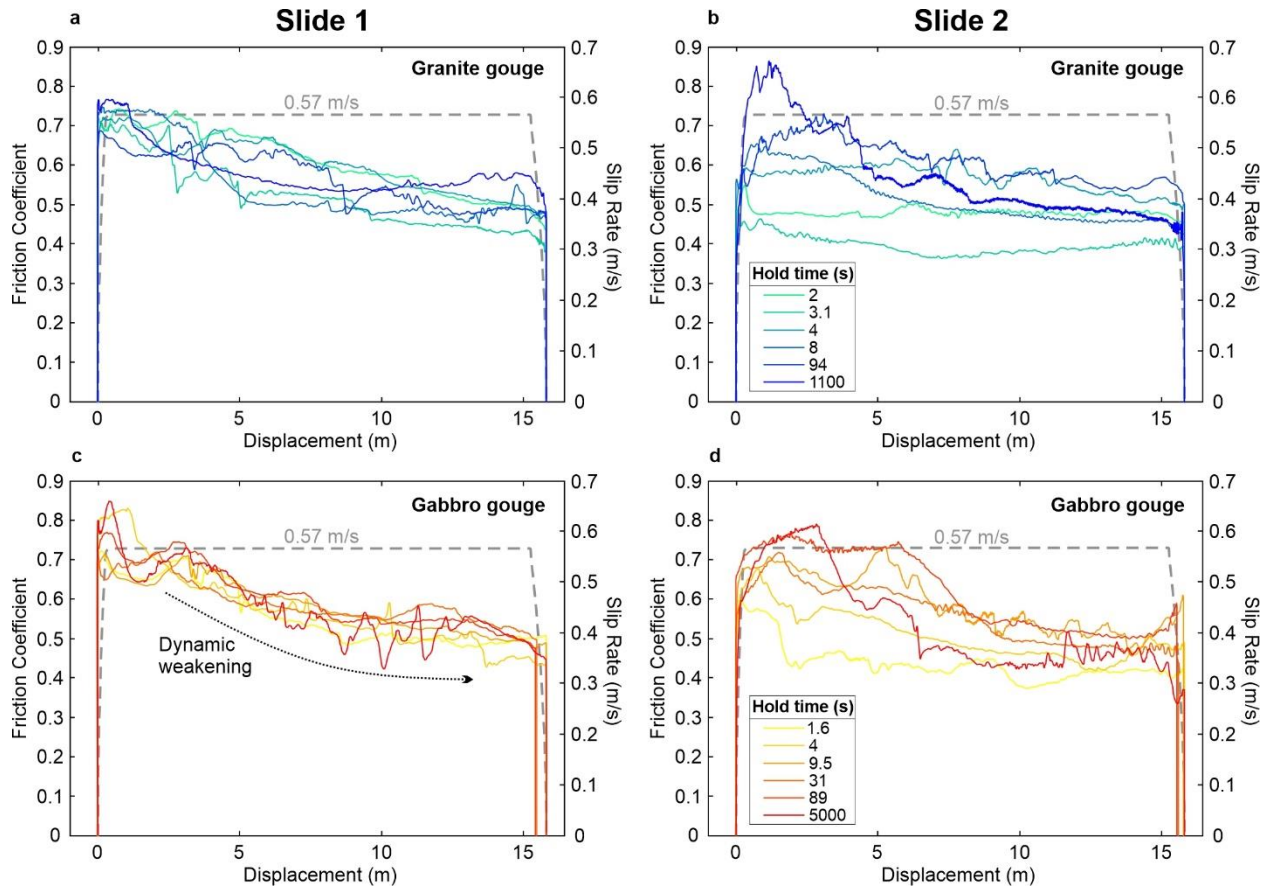
174 (SPECTRUM ONE, Jobin Yvon Horiba). Spatial resolution is about 1 μm , and wavenumber resolution is
175 about 1 cm^{-1} . Frequencies of the Raman bands were calibrated by measuring silicon standards.

176

177 **3. Results**

178 ***3.1. Friction data***

179 The frictional strength evolution of the granite and gabbro gouge samples is shown in Figure 2 for
180 both sliding events in the SHS experiments. During the first high-velocity sliding event (slide 1) the gouge
181 layers experience dynamic weakening with the friction coefficient (μ) decreasing by ~ 0.25 , from a peak
182 value between 0.7-0.8, to a final value of ~ 0.5 after 15 m of slip (Fig. 2a and c). This amount of weakening
183 is comparable to previous experimental studies performed under similar normal stress and velocity
184 conditions (e.g., Seyler et al., 2020), with greater weakening (to $\mu \approx 0.2$) typically observed when gouges
185 are sheared under higher normal stresses (Pozzi et al., 2021; Seyler et al., 2020) or at faster sliding velocities
186 (Boulton et al., 2017; Yao et al., 2013) than in our experiments. During the static hold period between
187 sliding events in our experiments the gouge undergoes healing, with the peak friction of the second sliding
188 event (slide 2) being dependent on the duration of the hold period (Fig. 2b and d) – i.e., longer hold periods
189 lead to higher peak friction values. During slide 2, after reaching their respective peak friction values, the
190 gouge layers again experience dynamic weakening, returning to a final μ of ~ 0.5 after another 15 m of high-
191 velocity slip.



192

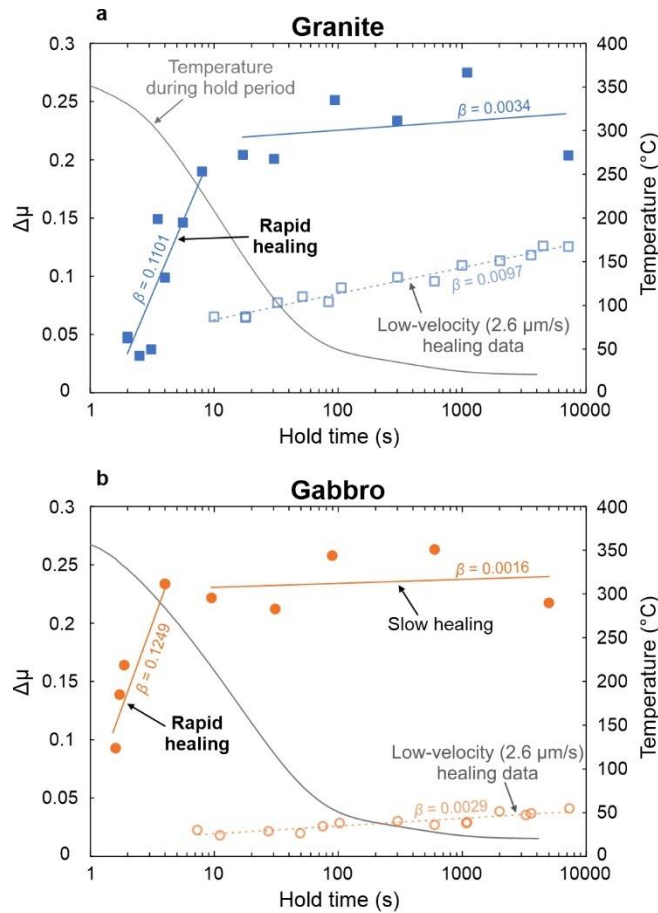
193 **Figure 2:** Example mechanical data from the two high-velocity sliding events in the slide-hold-slide
 194 experiments. The plots show the evolution of the friction coefficient with displacement for the granite gouge
 195 during (a) the first sliding event (slide 1), and (b) the second sliding event (slide 2). The same data are
 196 shown for the gabbro gouge in panels (c) and (d), respectively. The velocity-displacement history during
 197 the experiments is shown by the grey dashed line. The gouge layers all show similar dynamic weakening
 198 during slide 1, with the friction coefficient decreasing by ~ 0.25 after 15 m of displacement. The peak friction
 199 during slide 2 is controlled by the duration of the static hold time between the sliding events, with longer
 200 hold times leading to higher peak friction.

201

202 The gouge samples recover their strength rapidly during the static hold period, as shown in Figure
 203 3 where $\Delta\mu$ (the difference between the peak friction of slide 2 (μ_{p2}) and the final friction of slide 1 (μ_{f1}),

204 $\Delta\mu = \mu_{p2} - \mu_{f1}$; see also Fig. S2) is plotted against hold time. After around 20 s of static hold, the granite
205 gouge had recovered the majority of the strength it lost during slide 1, with the gabbro gouge healing even
206 more rapidly (<10 s of static hold). For comparison, healing data from low-velocity SHS experiments
207 performed on intact samples of granite and gabbro at slip rates of 2.6 $\mu\text{m/s}$ has been included in Figure 3
208 (see Methods for more details). The healing rate ($\beta = \Delta\mu/\Delta\log(t_h)$, where t_h is the hold time) is around
209 two orders of magnitude greater for the experiments performed at seismic slip velocities than those
210 performed at micrometer per second slip velocities (Fig. 3). After the initial rapid strength recovery in the
211 high-velocity tests, the healing rate decreased to a rate that is comparable to those observed in the low-
212 velocity SHS experiments.

213 A major difference between high-velocity and low-velocity SHS experiments is that during high-
214 velocity slip there is a large temperature increase caused by shear heating, which is much less significant
215 during sliding at low-velocity. In order to measure the temperature evolution in our high-velocity SHS
216 experiments, we placed thermocouples next to the upper surface of the gouge layer on the stationary side
217 of the fault in some experiments (see Methods). We recorded peak temperatures of around 350-400 $^{\circ}\text{C}$
218 during the high-velocity sliding events, with the temperature decaying as the samples cooled during the
219 hold period, returning to the ambient temperature in the laboratory after several minutes of static hold (Fig.
220 3). However, we find that the rapid frictional healing, which begins immediately after the initiation of the
221 hold period, occurred when the gouge layer was still relatively hot, at temperatures $>200^{\circ}\text{C}$ (Fig. 3).



222

223 **Figure 3:** Frictional healing data from the high-velocity SHS experiments. The slide-hold-slide parameter
 224 $\Delta\mu$ is plotted against hold time for (a) granite gouge and (b) gabbro gouge. The gouges experience rapid
 225 healing immediately after the initiation of the hold period; the healing rate then decreases to a rate
 226 comparable to those observed in low-velocity SHS experiments. Healing data from experiments performed
 227 at $2.6 \mu\text{m/s}$ has been included (hollow symbols) for comparison. The temperature evolution was monitored
 228 during the hold period (grey line); rapid healing occurs while the gouges are still relatively hot ($>200 \text{ }^\circ\text{C}$)
 229 after the high-velocity first sliding event.

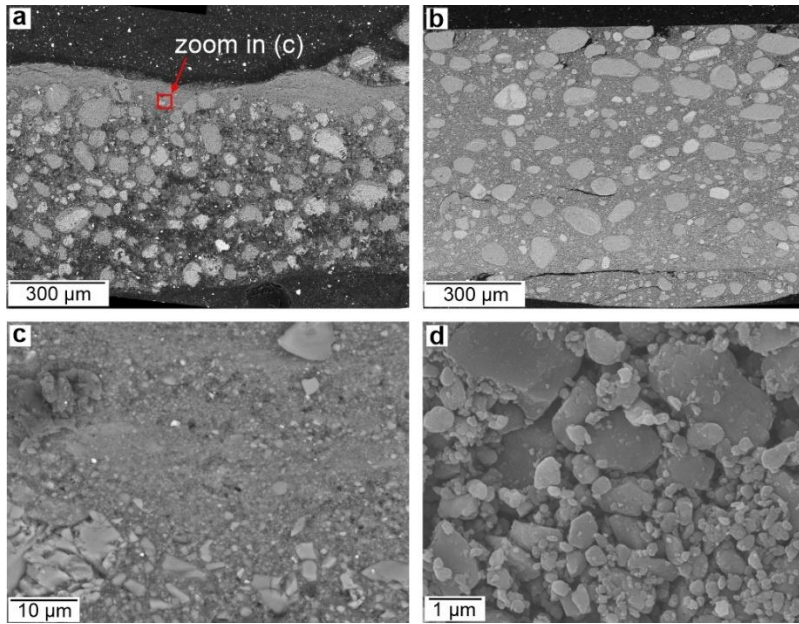
230

231 3.2. Microstructural analysis and Raman spectroscopy

232 We analyzed the microstructures of the sheared gouges by collecting backscatter electron (BSE)
 233 and secondary electron (SE) images using a JEOL JSM-6500F field emission scanning electron microscope

234 (FE-SEM). Fig. 4a-b shows BSE images of granite and gabbro gouge samples after the SHS experiments,
235 where the sheared layers have been cut perpendicular to the shear plane and parallel to the shearing direction
236 at a distance equal to $2/3$ of the sample radius. (Note that the gouge layers were vacuum impregnated with
237 a low-viscosity epoxy resin before being cut and polished ready for BSE imaging). The sheared gouges
238 display a texture of well-rounded larger relict grains surrounded by fine-grained highly comminuted
239 material, indicating that they have undergone a significant grain size reduction and particle rounding
240 when compared to the starting gouge material (see Fig. S3), with this likely occurring via mechanical
241 grinding (Sammis and Ben-Zion, 2008). In the granite gouge the deformation appears to be homogeneously
242 distributed across the layer (Fig. 4b), whereas the gabbro gouge displays evidence of a highly comminuted
243 localized zone at the boundary of the layer (Fig. 4a and c). Despite the apparent difference in localization
244 behavior between the different materials, their mechanical behavior is remarkably similar (Fig. 2),
245 suggesting that shear localization does not have a strong control on frictional strength evolution under these
246 experimental conditions. Our experiments were run under relatively low normal stress, previous studies
247 suggest that localization would become more prominent if the gouge layers were sheared under higher
248 normal stress (Bedford and Faulkner, 2021; Rempe et al., 2020), or if they were taken to greater shear
249 strains (Kaneki et al., 2020).

250



251

252 **Figure 4:** Backscatter electron images of (a) gabbro and (b) granite gouge layers recovered at the end of
 253 the SHS experiments. (c) Zoom of the localized zone within the gabbro gouge layer (from the red box in
 254 (a)). (d) Secondary electron image of the surface of the gabbro gouge layer showing the presence of sub-
 255 micron particles.

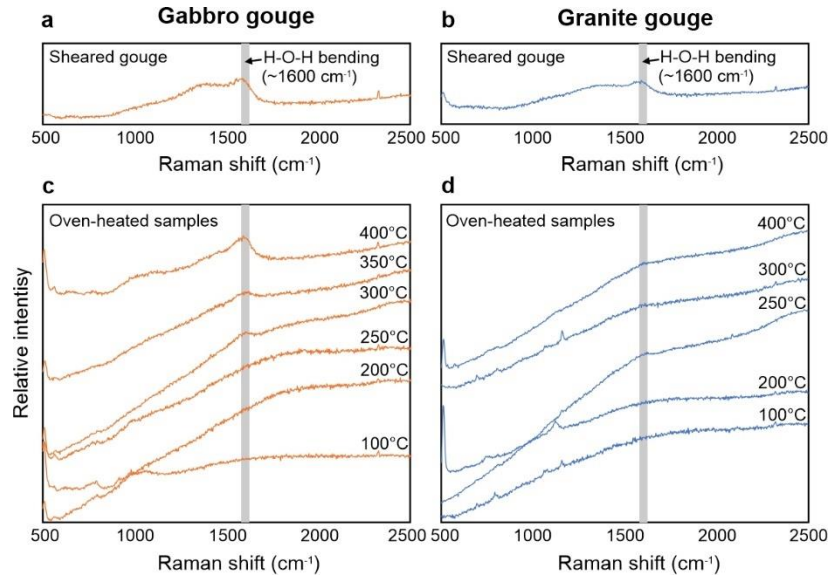
256

257 The rapid healing observed after sliding at seismic slip rates in our experiments (Fig. 3) must be
 258 caused by a strengthening of the frictional contacts in the gouge layer, possibly as a result of enhanced
 259 interfacial chemical bonding. To investigate further the possible causes of the rapid restrengthening, we
 260 analyzed the sheared gouges using Raman spectroscopy, as this provides information about the chemical
 261 structure of the gouge surface. We found that the gouges sheared at high-velocity all showed the appearance
 262 of a small broad peak in the Raman spectra at a wavenumber of $\sim 1600\text{ cm}^{-1}$ (Fig. 5a and b), which
 263 corresponds to the bending vibrational mode of water (Kronenberg, 1994) adsorbed on the surface of the
 264 gouge. The bending mode is one of the three characteristic molecular vibration modes of water (along with
 265 the symmetric and asymmetric stretching modes), where the atomic bond angles are compressed and
 266 expanded in an oscillatory manner. The Raman peak associated with the bending vibrational mode was not

267 observed for the starting material or for samples sheared at low sliding velocities, only for samples that had
268 been subjected to sliding at seismic slip rates.

269 We hypothesize that the switch in vibration mode of adsorbed water is caused by a change in
270 chemical bonding on the gouge surface, potentially induced by elevated temperatures during high-velocity
271 shearing, which could be responsible for the rapid healing observed in the SHS experiments (Fig. 3). To
272 investigate this further, we heated undeformed samples of granite and gabbro in an oven to different
273 temperatures (leaving them for ~20 minutes at the target temperature), the samples were then removed from
274 the oven and left to cool at room atmosphere conditions (i.e., the same cooling conditions that the gouge
275 layers experienced during the hold period of the SHS experiments). We analyzed the oven-heated samples
276 using Raman spectroscopy and found the appearance of a small broad peak at $\sim 1600\text{ cm}^{-1}$ for samples that
277 had been heated to temperatures $\geq 250\text{ }^{\circ}\text{C}$ (Fig. 5c and d), which is similar to the temperatures that the gouge
278 layers experienced during high-velocity shearing where a similar Raman peak was observed (Fig. 5a and
279 b) and also the temperature conditions where rapid healing occurred (Fig. 3). We note that the size of the
280 adsorbed water peak in the oven-heated samples is often less than observed for the sheared gouge samples
281 (particularly for granite), which may be a result the sheared gouges having a much greater surface area due
282 to the presence of nanoparticles (Fig. 4d), producing a stronger Raman signal.

283



284

285 **Figure 5:** Raman spectra of the surface of the sheared gabbro (e) and granite (f) layers at the end of the
 286 SHS experiments. Both show a broad peak at a wavenumber of $\sim 1600\text{ cm}^{-1}$, indicating the bending
 287 vibrational mode of H-O-H. Panels (g) and (h) show Raman spectra for undeformed gabbro and granite
 288 samples heated to different temperatures in an oven and then left to cool under atmospheric humidity
 289 conditions. The broad peak at 1600 cm^{-1} only appears in samples that have been heated to temperatures
 290 $\geq 250\text{ }^{\circ}\text{C}$.

291

292 4. Discussion

293 4.1. Rapid fault healing

294 The frictional strength data from our high-velocity SHS experiments show that the fault gouges heal
 295 rapidly during static hold periods after shearing at seismic slip rates, in comparison to typical healing rates
 296 observed in low-velocity SHS experiments performed at micrometer-per-second slip rates (Carpenter et al.,
 297 2016; Dieterich, 1972; Marone, 1997; Marone and Saffer, 2015) (Fig. 3). The rapid healing rates we observe
 298 for the granite and gabbro gouges in our study are a similar order to those observed in previous high-velocity
 299 SHS experiments on clay-carbonate-bearing gouges from the Longmenshan fault system (sheared at 0.8
 300 MPa normal stress and a slip rate of 1.4 m/s (Yao et al., 2013)), suggesting that rapid healing after high-

301 velocity slip may be a universal phenomenon that is largely insensitive to the lithology of the fault materials.
302 Elevated healing rates have also been observed in experiments performed at subseismic slip rates (on the
303 order of a few millimeters-per-second (e.g., Di Toro et al., 2004; Goldsby and Tullis, 2002)), however the
304 healing rates in these experiments are an order of magnitude lower than we observe in our experiments at
305 seismic slip velocities.

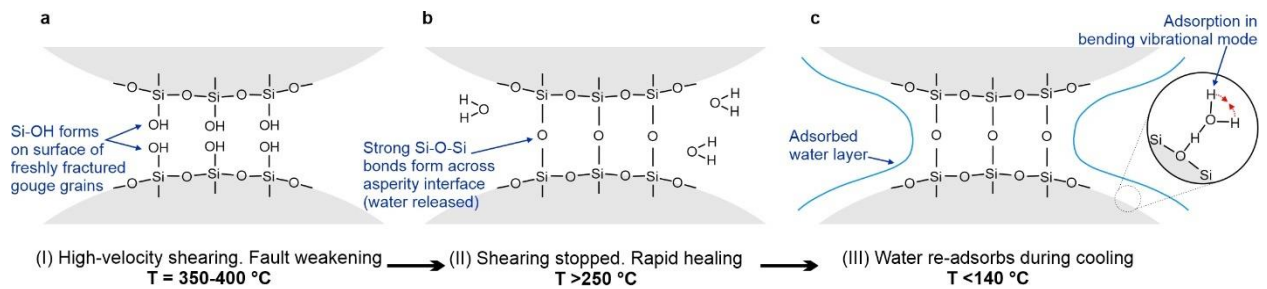
306 Dynamic weakening during the high-velocity shearing events in our experiments (Fig. 2) is likely
307 caused by a combination of flash heating at asperity contacts (Rice, 2006) and the formation of amorphous
308 wear materials in the gouge (Rowe et al., 2019). X-ray diffraction analysis of the sheared gouges confirms
309 the presence of amorphous material that was not present in the starting materials (Fig. S4). The
310 microstructures of the sheared gouges (Fig. 4) show no evidence of other weakening mechanisms that have
311 been reported in previous studies such as frictional melting (Hirose and Shimamoto, 2005), silica-gel
312 formation (Goldsby and Tullis, 2002) or grain-size sensitive flow (De Paola et al., 2015; Pozzi et al., 2021).
313 Fault restrengthening during the hold periods is likely caused by the reformation of bonds at asperity
314 contacts in the gouge material. There are two prevailing hypotheses for the time-dependent strengthening
315 of frictional contacts during fault healing: (i) an increase in real contact area by asperity creep (Dieterich
316 and Kilgore, 1994), often referred to as the contact ‘quantity’ hypothesis, or (ii) the formation of chemical
317 bonds across the asperity interface (Li et al., 2011; Thom et al., 2018), often referred to as the contact
318 ‘quality’ hypothesis.

319 If we first consider asperity creep, it is plausible that this process would be more active after seismic
320 slip, as creep is temperature-sensitive and the rapid healing we observe occurs immediately after high-
321 velocity slip while the gouge is still relatively hot (>200 °C, Fig. 3). The likely mechanisms that could
322 facilitate asperity creep are either solution-transfer processes (Rutter, 1983) or indentation creep (Scholz
323 and Engelder, 1976). Solution-transfer is unlikely to be a dominant mechanism in our experiments as they
324 were run without a pore-fluid (i.e., room atmosphere conditions), therefore there is no solute to transfer
325 chemical species. Furthermore, previous fault healing experiments under hydrothermal conditions, where

326 solution-transfer processes are operative, show complex healing behavior (Jeppson and Lockner, 2022;
327 Karner et al., 1997; Nakatani and Scholz, 2004; van den Ende and Niemeijer, 2019) that is quite different
328 to the healing trends we observe in our data (Fig. 3). Indentation creep can operate under atmospheric
329 conditions in the absence of a pore-fluid (Frye and Marone, 2002), however, although previous low-velocity
330 fault healing experiments at elevated temperatures (up to 550°C) under room humidity conditions indicate
331 some temperature-dependence on healing rate (Mitchell et al., 2013; Nakatani, 2001), the effect is relatively
332 minor (for intact granite Mitchell et al., (2013) found that β increases from 0.016 at room temperature to
333 0.021 at 500°C) and insufficient to explain the rapid healing in our experiments. It is therefore unlikely that
334 an increase in the real contact area via asperity creep is the cause of the rapid restrengthening we observe
335 during the static hold periods.

336 Alternatively, rapid healing may be caused by enhanced chemical bonding across contacting
337 asperity interfaces. Our Raman data reveal a change in chemical bonding on the surface of the gouges
338 sheared at high-velocity, with a switch in the vibrational mode of adsorbed water to the H-O-H bending
339 mode, which only occurs after sample has been heated to temperatures ≥ 250 °C (Fig. 5c-d). Although we
340 observe a change in adsorbed water properties, we do not expect the adsorbed water itself to be responsible
341 for the rapid healing, as rapid healing occurs at temperatures > 200 °C (Fig. 3) where water would be in the
342 vapor state and desorbed from the gouge surface (Reches and Lockner, 2010). Instead, we hypothesize that
343 the rapid healing is a result of hydrogen bonding on the surface of the sheared gouge materials, which
344 subsequently causes water to re-adsorb in the bending vibrational mode once the gouge has cooled to
345 sufficiently low temperatures (< 140 °C) (Reches and Lockner, 2010) during the hold period. Hydrogen
346 bonding can arise between hydroxylated silanol (Si-OH) surfaces (Michalske and Fuller, 1985), which are
347 readily formed on freshly cleaved surfaces of silicate materials during frictional slip (Hirose et al., 2011;
348 Kronenberg, 1994; Rowe et al., 2019) (Fig. 6a). Once slip has stopped, the formation of hydrogen bonds
349 between silanol surfaces can take place on very short timescales ($< 10^{-2}$ s) (Liu and Szlufarska, 2012).
350 Therefore, if hydrogen bonding occurs during the first few seconds of static hold in our experiments, it

351 could be responsible for the rapid increase in friction we observe. Furthermore, at elevated temperatures,
 352 like those produced by shear heating in our experiments, silanol groups on opposite sides of an asperity
 353 interface can react to form strong covalent siloxane (Si-O-Si) bonds (Shioji et al., 2001; Vigil et al., 1994)
 354 (Fig. 6b). Previous molecular dynamics simulations of silica-silica interfaces have shown that siloxane bond
 355 formation provides a plausible explanation for frictional healing, with frictional strength being
 356 approximately proportional to the number of siloxane bonds (Li et al., 2014) and the kinetics of interfacial
 357 bond formation leading to a logarithmic time-dependent increase in strength (Liu and Szlufarska, 2012), as
 358 observed in SHS experiments (Fig. 3). Therefore, we postulate that rapid healing after high-velocity slip is
 359 caused by either hydrogen or siloxane bond formation (or a combination of both) at asperity contacts in the
 360 sheared gouges. Once the gouge has cooled to sufficiently low temperature water will re-adsorb (Reches
 361 and Lockner, 2010) (Fig. 6c). The vibrational motions of water molecules are sensitive to local hydrogen
 362 bonding on the adsorbent surface (Kronenberg, 1994; Shioji et al., 2001), thus the switch to the H-O-H
 363 bending mode we observe on the sheared gouges likely results from changes in the hydrogen bonding on
 364 the gouge surface that occur during/after high-velocity slip while the gouge is still hot, hence why the
 365 change in adsorbed water properties is only observed in samples that have been heated to temperatures
 366 $>250\text{ }^{\circ}\text{C}$ (Fig. 5c-d) and not in the samples sheared at low velocity where the temperature increase was low.
 367



369 **Figure 6:** Schematic cartoon showing the evolution of chemical bonding during and after high-velocity
 370 slip. (a) Silanol bonds (Si-OH) form on freshly fractured gouge surfaces during high-velocity slip. During
 371 the hold period, once fault slip has ceased, we hypothesize that rapid healing occurs as a result of either

372 *hydrogen bonding between adjacent silanol surfaces, or (b) the formation of strong siloxane bonds across*
373 *the asperity interface. (c) Once the gouge has cooled to temperatures <140 °C during the hold period,*
374 *water re-adsorbs onto the surface in the bending vibrational mode.*

375

376 ***4.2. Implications for fault strength evolution and earthquake recurrence***

377 Regardless of the underlying restrengthening mechanism, our data clearly show that fault materials
378 heal rapidly after seismic slip, which has important implications for our understanding of the earthquake
379 cycle. Rapid healing may explain why geophysical observations suggest faults can regain their strength
380 early during interseismic periods after large earthquakes (Tadokoro and Ando, 2002; Xue et al., 2013).
381 Fast-acting healing mechanisms, like those in operation during our experiments, potentially also operate
382 during coseismic slip on natural faults, particularly when slip occurs heterogeneously along the fault such
383 as during the propagation of pulse-like ruptures (Heaton, 1990; Lambert et al., 2021; Wang and Barbot,
384 2023). The passage of a rupture pulse requires rapid healing in the just-slipped portions of the fault (Perrin
385 et al., 1995), in order for them to stay locked and prevent further slip as they are reloaded by waves from
386 the actively slipping regions elsewhere along the fault. Results from recent dynamic rupture experiments
387 further highlight the complex interplay between rapid weakening and healing processes that occur in gouge
388 samples during dynamic rupture propagation (Rubino et al., 2022).

389 Rapid fault strength recovery immediately following a seismic event suggests that earthquake
390 recurrence is not necessarily controlled by continuous restrengthening over time during interseismic
391 periods. Instead, if the majority of strength is recovered early during the interseismic period, as implied by
392 our results, then earthquake recurrence on natural faults may be more strongly controlled by far-field
393 tectonic loading (i.e., when the buildup of stress applied to the fault exceeds the strength an earthquake may
394 occur). Alternatively, other time-dependent processes in operation during interseismic periods may
395 influence earthquake recurrence. For example, over typical recurrence intervals of hundreds of years, fault
396 cohesion will also increase by longer timescale processes such as a pressure solution (Muhuri et al., 2003;

397 Tenthorey and Cox, 2006; van den Ende and Niemeijer, 2019). The resulting increase in cohesion and
398 lithification of the fault gouge will not only contribute to the fault strength evolution, but will also influence
399 the frictional stability of the gouge materials, with more cohesive materials often displaying rate-weakening
400 behavior required for earthquake nucleation (Ikari and Hüpers, 2021; Roesner et al., 2020). It is plausible
401 that transitions from rate-strengthening to rate-weakening behavior may occur as the gouge materials
402 become more lithified during interseismic periods, potentially leading to earthquake recurrence once the
403 frictional properties have evolved to state that promotes earthquake nucleation and unstable slip.

404

405 **5. Conclusions**

406 In summary, we find that faults regain their strength rapidly after experiencing dynamic weakening
407 during seismic slip. After the initial rapid increase in strength, the healing rate decreases to a rate that is
408 comparable to those observed in low-velocity friction experiments. Rapid healing occurs while the gouge
409 is still hot from shear heating, and is likely promoted by enhanced chemical bonding across contacting
410 asperity interfaces. Further experimental and theoretical studies are needed to investigate the kinetics of
411 interfacial reactions over the range of stress, temperature and pore fluid conditions that faults experience
412 during and after earthquake slip, to understand better strength recovery at seismogenic depths. Our findings
413 motivate further study aimed at the quantification of rapid healing mechanisms and incorporation into
414 larger-scale constitutive laws for modelling dynamic fault processes, to provide insight into the driving
415 mechanisms of earthquake rupture and arrest, and hence seismic hazard.

416

417 **Acknowledgments**

418 We are grateful to T. Suzuki and O. Tadai for technical support with the experiments and analyses. This
419 work was supported by a Japan Society for the Promotion of Science (JSPS) International Research
420 Fellowship and JSPS KAKENHI Grant Numbers JP20F20786 and JP19K21907. The associated

421 experimental data files for this research can be accessed at:

422 <https://data.mendeley.com/datasets/rw3ndtwkgt/1>

423

424 **References**

425 Bedford, J.D., Faulkner, D.R., 2021. The role of grain size and effective normal stress on localization and
426 the frictional stability of simulated quartz gouge. *Geophys. Res. Lett.* 48, e2020GL092023.

427 <https://doi.org/10.1029/2020gl092023>

428 Boulton, C., Yao, L., Faulkner, D.R., Townend, J., Toy, V.G., Sutherland, R., Ma, S., Shimamoto, T.,
429 2017. High-velocity frictional properties of Alpine Fault rocks: Mechanical data, microstructural
430 analysis, and implications for rupture propagation. *J. Struct. Geol.* 97, 71–92.

431 <https://doi.org/10.1016/j.jsg.2017.02.003>

432 Carpenter, B.M., Ikari, M.J., Marone, C., 2016. Laboratory observations of time-dependent frictional
433 strengthening and stress relaxation in natural and synthetic fault gouges. *J. Geophys. Res. Solid
434 Earth* 121, 1183–1201. <https://doi.org/10.1002/2015JB012136>

435 De Paola, N., Holdsworth, R.E., Viti, C., Collettini, C., Bullock, R., 2015. Can grain size sensitive flow
436 lubricate faults during the initial stages of earthquake propagation? *Earth Planet. Sci. Lett.* 431, 48–
437 58. <https://doi.org/10.1016/j.epsl.2015.09.002>

438 Di Toro, G., Goldsby, D.L., Tullis, T.E., 2004. Friction falls towards zero in quartz rock as slip velocity
439 approaches seismic rates. *Nature* 427, 436–439. <https://doi.org/10.1038/nature02249>

440 Di Toro, G., Han, R., Hirose, T., De Paola, N., Nielsen, S., Mizoguchi, K., Ferri, F., Cocco, M.,
441 Shimamoto, T., 2011. Fault lubrication during earthquakes. *Nature* 471, 494–498.

442 <https://doi.org/10.1038/nature09838>

443 Dieterich, J.H., 1972. Time-dependent friction in rocks. *J. Geophys. Res.* 77, 3690–3697.

444 <https://doi.org/10.1029/JB077i020p03690>

445 Dieterich, J.H., Kilgore, B.D., 1994. Direct observation of frictional contacts: New insights for state-
446 dependent properties. *Pure Appl. Geophys.* 143, 283–302. <https://doi.org/10.1007/BF00874332>

447 Frye, K.M., Marone, C., 2002. Effect of humidity on granular friction at room temperature. *J. Geophys.*
448 *Res.* 107, 2309. <https://doi.org/10.1029/2001jb000654>

449 Goldsby, D.L., Tullis, T.E., 2002. Low frictional strength of quartz rocks at subseismic slip rates.
450 *Geophys. Res. Lett.* 29, 1844. <https://doi.org/10.1029/2002GL015240>

451 Han, R., Shimamoto, T., Hirose, T., Ree, J.H., Ando, J., 2007. Ultralow friction of carbonate faults caused
452 by thermal decomposition. *Science* (80-.). 316, 878–881. <https://doi.org/10.1126/science.1139763>

453 Harbord, C., Brantut, N., Spagnuolo, E., Di Toro, G., 2021. Fault friction during simulated seismic slip
454 pulses. *J. Geophys. Res. Solid Earth* 126, e2021JB022149. <https://doi.org/10.1029/2021JB022149>

455 Heaton, T.H., 1990. Evidence for and implications of self-healing pulses of slip in earthquake rupture.
456 *Phys. Earth Planet. Inter.* 64, 1–20. [https://doi.org/10.1016/0031-9201\(90\)90002-F](https://doi.org/10.1016/0031-9201(90)90002-F)

457 Hirose, T., Kawagucci, S., Suzuki, K., 2011. Mechanoradical H₂ generation during simulated faulting:
458 Implications for an earthquake-driven subsurface biosphere. *Geophys. Res. Lett.* 38, L17303.
459 <https://doi.org/10.1029/2011GL048850>

460 Hirose, T., Shimamoto, T., 2005. Growth of molten zone as a mechanism of slip weakening of simulated
461 faults in gabbro during frictional melting. *J. Geophys. Res.* 110, B05202.
462 <https://doi.org/10.1029/2004JB003207>

463 Hunfeld, L.B., Chen, J., Niemeijer, A.R., Ma, S., Spiers, C.J., 2021. Seismic slip-pulse experiments
464 simulate induced earthquake rupture in the Groningen gas field. *Geophys. Res. Lett.* 48,
465 e2021GL092417. <https://doi.org/10.1029/2021GL092417>

466 Ikari, M.J., Hüpers, A., 2021. Velocity-weakening friction induced by laboratory-controlled lithification.

467 Earth Planet. Sci. Lett. 554, 116682. <https://doi.org/10.1016/j.epsl.2020.116682>

468 Jeppson, T., Lockner, D., 2022. Impact of fluid-rock interaction on strength and hydraulic transmissivity
469 evolution in shear fractures under hydrothermal conditions, in: 47th Workshop on Geothermal
470 Reservoir Engineering. Stanford, California.

471 Kanamori, H., Allen, C.R., 1986. Earthquake repeat time and average stress drop, in: Das, S., Boatwright,
472 J., Scholz, C.H. (Eds.), Earthquake Source Mechanics. American Geophysical Union, Washington
473 D.C., pp. 227–235. <https://doi.org/10.1029/GM037p0227>

474 Kaneki, S., Oohashi, K., Hirono, T., Noda, H., 2020. Mechanical amorphization of synthetic fault gouges
475 during rotary-shear friction experiments at subseismic to seismic slip velocities. *J. Geophys. Res.*
476 *Solid Earth* 125, e2020JB019956. <https://doi.org/10.1029/2020JB019956>

477 Karner, S.L., Marone, C., Evans, B., 1997. Laboratory study of fault healing and lithification in simulated
478 fault gouge under hydrothermal conditions. *Tectonophysics* 277, 41–55.
479 [https://doi.org/10.1016/S0040-1951\(97\)00077-2](https://doi.org/10.1016/S0040-1951(97)00077-2)

480 Kronenberg, A.K., 1994. Hydrogen speciation and chemical weakening of quartz, in: Heaney, P.J.,
481 Prewitt, C.T., Gibbs, G. V (Eds.), *Silica: Physical Behaviour, Geochemistry and Materials*
482 *Applications*. Mineralogical Society of America, pp. 123–176.

483 Lambert, V., Lapusta, N., Perry, S., 2021. Propagation of large earthquakes as self-healing pulses or mild
484 cracks. *Nature* 591, 252–258. <https://doi.org/10.1038/s41586-021-03248-1>

485 Li, A., Liu, Y., Szlufarska, I., 2014. Effects of interfacial bonding on friction and wear at silica/silica
486 interfaces. *Tribol. Lett.* 56, 481–490. <https://doi.org/10.1007/s11249-014-0425-x>

487 Li, Q., Tullis, T.E., Goldsby, D., Carpick, R.W., 2011. Frictional ageing from interfacial bonding and the
488 origins of rate and state friction. *Nature* 480, 233–236. <https://doi.org/10.1038/nature10589>

489 Li, Y.-G., Chen, P., Cochran, E.S., Vidale, J.E., Burdette, T., 2006. Seismic evidence for rock damage

490 and healing on the San Andreas Fault associated with the 2004 M 6.0 Parkfield earthquake. *Bull.*
491 *Seismol. Soc. Am.* 96, S349–S363. <https://doi.org/10.1785/0120050803>

492 Liu, Y., Szlufarska, I., 2012. Chemical origins of frictional aging. *Phys. Rev. Lett.* 109.
493 <https://doi.org/10.1103/PhysRevLett.109.186102>

494 Magen, Y., Ziv, A., Inbal, A., Baer, G., Hollingsworth, J., 2020. Fault rerupture during the July 2019
495 Ridgecrest earthquake pair from joint slip inversion of InSAR, optical imagery, and GPS. *Bull.*
496 *Seismol. Soc. Am.* 110, 1627–1643. <https://doi.org/10.1785/0120200024>

497 Marone, C., 1997. On the rate of frictional healing and the constitutive law for time- and slip-dependent
498 friction. *Int. J. Rock Mech. Min. Sci.* 34, 187.e1-187.e17. [https://doi.org/10.1016/S1365-](https://doi.org/10.1016/S1365-1609(97)00054-3)
499 [1609\(97\)00054-3](https://doi.org/10.1016/S1365-1609(97)00054-3)

500 Marone, C., Saffer, D.M., 2015. The mechanics of frictional healing and slip instability during the seismic
501 cycle, in: Schubert, G. (Ed.), *Treatise on Geophysics*. Elsevier, pp. 111–138.
502 <https://doi.org/10.1016/B978-0-444-53802-4.00092-0>

503 Marone, C., Vidale, J.E., Ellsworth, W.L., 1995. Fault healing inferred from time dependent variations in
504 source properties of repeating earthquakes. *Geophys. Res. Lett.* 22, 3095–3098.
505 <https://doi.org/10.1029/95GL03076>

506 McLaskey, G.C., Thomas, A.M., Glaser, S.D., Nadeau, R.M., 2012. Fault healing promotes high-
507 frequency earthquakes in laboratory experiments and on natural faults. *Nature* 491, 101–104.
508 <https://doi.org/10.1038/nature11512>

509 Michalske, T.A., Fuller, E.R., 1985. Closure and repropagation of healed cracks in silicate glass. *J. Am.*
510 *Ceram. Soc.* 68, 586–590. <https://doi.org/10.1111/j.1151-2916.1985.tb16160.x>

511 Mitchell, E.K., Fialko, Y., Brown, K.M., 2013. Temperature dependence of frictional healing of Westerly
512 granite: Experimental observations and numerical simulations. *Geochemistry, Geophys. Geosystems*
513 14, 567–582. <https://doi.org/10.1029/2012GC004241>

514 Muhuri, S.K., Dewers, T.A., Scott Jr., T.E., Reches, Z., 2003. Interseismic fault strengthening and
515 earthquake-slip instability: Friction or cohesion? *Geology* 31, 881–884.
516 <https://doi.org/10.1130/G19601.1>

517 Nakatani, M., 2001. Conceptual and physical clarification of rate and state friction: Frictional sliding as a
518 thermally activated rheology. *J. Geophys. Res.* 106, 13347–13380.
519 <https://doi.org/10.1029/2000JB900453>

520 Nakatani, M., Scholz, C.H., 2004. Frictional healing of quartz gouge under hydrothermal conditions: 1.
521 Experimental evidence for solution transfer healing mechanism. *J. Geophys. Res.* 109, B07201.
522 <https://doi.org/10.1029/2001JB001522>

523 Pei, S., Niu, F., Ben-Zion, Y., Sun, Q., Liu, Y., Xue, X., Su, J., Shao, Z., 2019. Seismic velocity reduction
524 and accelerated recovery due to earthquakes on the Longmenshan fault. *Nat. Geosci.* 12, 387–392.
525 <https://doi.org/10.1038/s41561-019-0347-1>

526 Perrin, G., Rice, J.R., Zheng, G., 1995. Self-healing slip pulse on a frictional surface. *J. Mech. Phys.*
527 *Solids* 43, 1461–1495. [https://doi.org/10.1016/0022-5096\(95\)00036-I](https://doi.org/10.1016/0022-5096(95)00036-I)

528 Pozzi, G., De Paola, N., Nielsen, S.B., Holdsworth, R.E., Tesei, T., Thieme, M., Demouchy, S., 2021.
529 Coseismic fault lubrication by viscous deformation. *Nat. Geosci.* 14, 437–442.
530 <https://doi.org/10.1038/s41561-021-00747-8>

531 Proctor, B.P., Mitchell, T.M., Hirth, G., Goldsby, D., Zorzi, F., Platt, J.D., Di Toro, G., 2014. Dynamic
532 weakening of serpentinite gouges and bare surfaces at seismic slip rates. *J. Geophys. Res. Solid*
533 *Earth* 119, 8107–8131. <https://doi.org/10.1002/2014JB011057>

534 Reches, Z., Lockner, D.A., 2010. Fault weakening and earthquake instability by powder lubrication.
535 *Nature* 467, 452–455. <https://doi.org/10.1038/nature09348>

536 Rempe, M., Di Toro, G., Mitchell, T.M., Smith, S.A.F., Hirose, T., Renner, J., 2020. Influence of
537 effective stress and pore fluid pressure on fault strength and slip localization in carbonate slip zones.

538 J. Geophys. Res. Solid Earth 125, e2020JB019805. <https://doi.org/10.1029/2020JB019805>

539 Rice, J.R., 2006. Heating and weakening of faults during earthquake slip. J. Geophys. Res. 111.
540 <https://doi.org/10.1029/2005JB004006>

541 Roesner, A., Ikari, M.J., Saffer, D.M., Stanislawski, K., Eijsink, A.M., Kopf, A.J., 2020. Friction
542 experiments under in-situ stress reveal unexpected velocity-weakening in Nankai accretionary prism
543 samples. Earth Planet. Sci. Lett. 538. <https://doi.org/10.1016/j.epsl.2020.116180>

544 Rowe, C.D., Lamothe, K., Rempe, M., Andrews, M., Mitchell, T.M., Di Toro, G., White, J.C., Aretusini,
545 S., 2019. Earthquake lubrication and healing explained by amorphous nanosilica. Nat. Commun. 10,
546 1–11. <https://doi.org/10.1038/s41467-018-08238-y>

547 Rubino, V., Lapusta, N., Rosakis, A.J., 2022. Intermittent lab earthquakes in dynamically weakening fault
548 gouge. Nature 606, 922–929. <https://doi.org/10.1038/s41586-022-04749-3>

549 Rutter, E.H., 1983. Pressure solution in nature, theory and experiment. J. Geol. Soc. London. 140, 725–
550 740. <https://doi.org/10.1144/gsjgs.140.5.0725>

551 Sammis, C.G., Ben-Zion, Y., 2008. Mechanics of grain-size reduction in fault zones. J. Geophys. Res.
552 Solid Earth 113. <https://doi.org/10.1029/2006JB004892>

553 Scholz, C.H., Aviles, C.A., Wesnousky, S.G., 1986. Scaling differences between large interplate and
554 intraplate earthquakes. Bull. Seismol. Soc. Am. 76, 65–70.
555 <https://doi.org/10.1785/BSSA0760010065>

556 Scholz, C.H., Engelder, J.T., 1976. The role of asperity indentation and ploughing in rock friction - I.
557 Asperity creep and stick-slip. Int. J. Rock Mech. Min. Sci. Geomech. Abstr. 13, 149–154.
558 [https://doi.org/10.1016/0148-9062\(76\)90819-6](https://doi.org/10.1016/0148-9062(76)90819-6)

559 Seyler, C.E., Kirkpatrick, J.D., Savage, H.M., Hirose, T., Faulkner, D.R., 2020. Rupture to the trench?
560 Frictional properties and fracture energy of incoming sediments at the Cascadia subduction zone.

561 Earth Planet. Sci. Lett. 546, 116413. <https://doi.org/10.1016/j.epsl.2020.116413>

562 Shioji, S., Kawaguchi, M., Hayashi, Y., Tokami, K., Yamamoto, H., 2001. Rehydroxylation of
563 dehydrated silica surfaces by water vapor adsorption. *Adv. Powder Technol.* 12, 331–342.
564 <https://doi.org/10.1163/156855201750537884>

565 Sone, H., Shimamoto, T., 2009. Frictional resistance of faults during accelerating and decelerating
566 earthquake slip. *Nat. Geosci.* 2, 705–708. <https://doi.org/10.1038/ngeo637>

567 Tadokoro, K., Ando, M., 2002. Evidence for rapid fault healing derived from temporal changes in S wave
568 splitting. *Geophys. Res. Lett.* 29, 1047. <https://doi.org/10.1029/2001GL013644>

569 Tanikawa, W., Mukoyoshi, H., Tadaï, O., 2012. Experimental investigation of the influence of slip
570 velocity and temperature on permeability during and after high-velocity fault slip. *J. Struct. Geol.*
571 38, 90–101. <https://doi.org/10.1016/j.jsg.2011.08.013>

572 Tenthorey, E., Cox, S.F., 2006. Cohesive strengthening of fault zones during the interseismic period: An
573 experimental study. *J. Geophys. Res.* 111. <https://doi.org/10.1029/2005JB004122>

574 Thom, C.A., Carpick, R.W., Goldsby, D.L., 2018. Constraints on the physical mechanism of frictional
575 aging from nanoindentation. *Geophys. Res. Lett.* 45, 13306–13311.
576 <https://doi.org/10.1029/2018GL080561>

577 Tsutsumi, A., Shimamoto, T., 1997. High-velocity frictional properties of gabbro. *Geophys. Res. Lett.* 24,
578 699–702. <https://doi.org/10.1029/97GL00503>

579 Tullis, T.E., 2015. Mechanisms for friction of rock at earthquake slip rates, in: Schubert, G. (Ed.),
580 *Treatise on Geophysics*. Elsevier, pp. 139–159. [https://doi.org/10.1016/B978-0-444-53802-4.00073-](https://doi.org/10.1016/B978-0-444-53802-4.00073-7)
581 [7](https://doi.org/10.1016/B978-0-444-53802-4.00073-7)

582 van den Ende, M.P.A., Niemeijer, A.R., 2019. An investigation into the role of time-dependent cohesion
583 in interseismic fault restrengthening. *Sci. Rep.* 9, 9894. <https://doi.org/10.1038/s41598-019-46241-5>

584 Vidale, J.E., Ellsworth, W.L., Cole, A., Marone, C., 1994. Variations in rupture process with recurrence
585 interval in a repeated small earthquake. *Nature* 368, 624–626. <https://doi.org/10.1038/368624a0>

586 Vigil, G., Xu, Z., Steinberg, S., Israelachvili, J., 1994. Interactions of silica surfaces. *J. Colloid Interface*
587 *Sci.* 165, 367–385. <https://doi.org/10.1006/jcis.1994.1242>

588 Violay, M., Passelegue, F., Spagnuolo, E., Di Toro, G., Cornelio, C., 2019. Effect of water and rock
589 composition on re-strengthening of cohesive faults during the deceleration phase of seismic slip
590 pulses. *Earth Planet. Sci. Lett.* 522, 55–64. <https://doi.org/10.1016/j.epsl.2019.06.027>

591 Wang, B., Barbot, S., 2023. Pulse-like ruptures, seismic swarms, and tremorgenic slow-slip events with
592 thermally activated friction. *Earth Planet. Sci. Lett.* 603, 117983.
593 <https://doi.org/10.1016/j.epsl.2022.117983>

594 Xue, L., Li, H.-B., Brodsky, E.E., Xu, Z.-Q., Kano, Y., Wang, H., Mori, J.J., Si, J.-L., Pei, J.-L., Zhang,
595 W., Yang, G., Sun, Z.-M., Huang, Y., 2013. Continuous permeability measurements record healing
596 inside the Wenchuan earthquake fault zone. *Science* (80-.). 340, 1555–1559.
597 <https://doi.org/10.1126/science.1237237>

598 Yao, L., Shimamoto, T., Ma, S., Han, R., Mizoguchi, K., 2013. Rapid postseismic strength recovery of
599 Pingxi fault gouge from the Longmenshan fault system: Experiments and implications for the
600 mechanisms of high-velocity weakening of faults. *J. Geophys. Res. Solid Earth* 118, 4547–4563.
601 <https://doi.org/10.1002/jgrb.50308>

602